Journal of the Mechanics and Physics of Solids, in press (2020)

Stress Effects on the Energy Barrier and Mechanisms of Cross-Slip in FCC Nickel

William P. Kuykendall, Yifan Wang and Wei Cai‡

Department of Mechanical Engineering, Stanford University, CA 94305-4040

Abstract. The energy barrier for homogeneous cross-slip of a screw dislocation in face-centered cubic (FCC) nickel is calculated using atomistic simulations as a function of the Escaig stress on the glide plane, the Escaig stress on the cross-slip plane, and the Schmid stress on the cross-slip plane. Two cross-slip mechanisms, Friedel-Escaig (FE) and Fleischer, are examined and their energy barriers are calculated for a large number of stress combinations. For each mechanism, the energy barrier as a function of three stress components can be reduced into a one-dimensional function of an effective stress. The stress domains in which FE and Fleischer mechanisms operate respectively are determined. The FE mechanism dominates when the Escaig stress on the glide plane (in the direction that reduces the stacking fault width) is the largest stress component. Increasing the Schmid stress and Escaig stress (in the direction that expands the stacking fault width) on the cross slip plane promotes the Fleischer mechanism. The cross slip energy barrier functions obtained here can be used as input functions for computing cross slip rates in mesoscale dislocation dynamics simulations.

‡ caiwei@stanford.edu

1. Introduction

Dislocation cross-slip occurs when a screw dislocation moves from its original slip plane (called the glide plane in the following) to a different one (called the cross-slip plane). This is usually driven by the stress acting on the dislocation and is aided by thermal fluctuations. The ability for screw dislocations to cross-slip in face-centered cubic (FCC) metals [1] is believed to be important for many different phenomena, including dislocation multiplication, pattern formation, dynamic recovery, and strain hardening [2, 3]. The rate at which cross-slip occurs, therefore, is an important input for mesoscale models, such as dislocation dynamics (DD) simulations [4]. Because cross-slip is a thermally activated process, the cross-slip rate is controlled by the activation (free energy) barrier, which depends on various conditions, including the local stress state around the screw dislocation, the presence of a jog or an intersecting dislocation, and so on. The multiplitude of factors influencing the activation barrier makes accurate prediction of the cross-slip rate a challenging task.

Both continuum models and atomistic simulations have been applied to understand the various factors that influence the activation barrier, including the presence of a jog [5], intersection with forest dislocations [6, 7, 8, 9, 10, 11, 12], and intersection with a free surface [13]. However, our understanding remains incomplete, even in the most idealized situation: that of "homogeneous" cross-slip of a single, straight screw dislocation. The term "homogeneous" here means the dislocation cross-slips in the bulk crystal without assistance from any other defects, such as jogs, intersecting dislocations, or surfaces. Even in this idealized case, the effects of stress, temperature, and material parameters on the cross-slip rate and mechanisms are still not well understood.

Several mechanisms have been proposed about how homogeneous cross-slip may occur. This work focuses on two mechanisms that have received most attention in the literature: the Friedel-Escaig (FE) mechanism and the Fleischer mechanism. In the FE mechanism [14, 15, 16], the two partial dislocations of the perfect screw dislocation first constrict to a point on the glide plane. From this initial constriction point, the perfect dislocation then re-dissociates into two partials on the cross-slip plane, creating two separate constrictions along the intersection line between the glide plane and cross-slip plane, as shown in Figure 1(a). Cross-slip then proceeds as the two constrictions move away from each other and the section of the dislocation residing on the cross-slip plane becomes longer. In the Fleischer mechanism [17], the leading partial dissociates into a Shockley partial dislocation on the cross-slip plane and a stair-rod dislocation at the intersection of the glide and cross-slip planes, as shown in Figure 1(b). In this way, the stacking fault continues on from the glide plane to the cross-slip plane without first constricting. Thus the activated state for the Fleischer mechanism contains a three-dimensional stacking fault structure.

Other mechanisms have been proposed for cross-slip, including the ones by Friedel [18], Yoshinaga and Horiuchi [19], Schoeck and Seeger [20], and Wolf [21]. The mechanisms presented by Friedel, Schoeck and Seeger, and Wolf are similar to the FE mechanism; they differ mainly in whether the initial constriction occurs at a point (as in FE) or along a

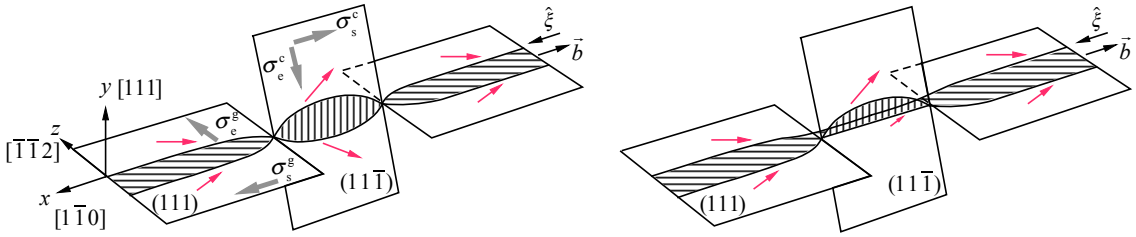

(a) Friedel-Escaig (FE) mechanism (b) Fleischer mechanism

Figure 1. Schematics of the two cross-slip mechanisms investigated. The dislocation line direction is in the positive x-direction, while the Burgers vector is in the negative x-direction (resulting in a left-handed screw dislocation). The (111) plane is the glide plane while the $(11\bar{1})$ plane is the cross-slip plane. Also shown are the Burgers vectors of the partial dislocations (pointing toward each other on the glide plane and away from each other on the cross-slip plane) and the directions of the Escaig and Schmid stresses on the glide and cross-slip planes. (a) The FE mechanism occurs by the partial dislocations first constricting to a point on the glide plane, then re-dissociating on the cross-slip plane, forming two constrictions that move apart. (b) The Fleischer mechanism occurs when the leading partial dissociates into a partial in the cross-slip plane and a stair rod dislocation at the intersection between the glide plane and cross-slip plane, creating a three-dimensional stacking fault structure.

line segment and whether or not the constricted section of the dislocation re-dissociates on the cross-slip plane. In the mechanism proposed by Yoshinaga and Horiuchi [19], after the dislocation moves onto the cross-slip plane, it then re-dissociates onto a plane parallel to the original glide plane, i.e. the dislocation undergoes double cross-slip. These mechanisms are not investigated in this paper. The assumption that we do not need to explicitly consider these possibilities may be justified as follows.

We employ an atomistic model and search for the minimum energy path (MEP) for cross-slip. The converged MEP (under a given stress state) provides a prediction of not only the energy barrier but also the cross-slip mechanism. The initial path at the beginning of the MEP search is constructed based on either the FE or the Fleischer mechanism. We found that if, say, the initial path is constructed based on the Fleischer mechanism, the converged MEP may turn out to represent the FE mechanism if the latter is the more preferred mechanism under the given stress state. In other words, the MEP search algorithm can, to some extent, identify the correct mechanism even if the initial guess was constructed incorrectly. Therefore, if an alternative mechanism were indeed more preferred than the FE and Fleischer mechanisms studied here, it should be possible (though not guaranteed), for the MEP algorithm to converge to such a mechanism. Nonetheless, the vast majority of the (over three hundred) simulations conducted in this work show either FE or Fleischer mechanisms when the energy barriers have converged.

A number of the cross-slip models were originally conceived using the line tension approximation [1]. The line tension model has the advantage that its equations can be solved much more quickly compared with the MEP search in an atomistic model. Unfortunately,

previous results [22] have shown that the line tension model is unable to reproduce the stress effects on the energy barrier predicted by the atomistic model. For example, when the line tension parameters are fitted to reproduce the effect of the Escaig stress on the glide plane (the component with the strongest effect on the energy barrier), the line tension model under-predicts the effects of two other stress components. Therefore, it seems necessary to use atomistic simulations to predict the effect of multiple stress components on the cross-slip energy barrier.

In Kang et al. [22], the effects of three stress components on the cross-slip energy barrier have been examined. These stress components are: the Escaig stress on the glide plane ($\sigma_{\mathrm{e}}^{\mathrm{g}}$), the Escaig stress on the cross-slip plane ($\sigma_{\mathrm{e}}^{\mathrm{c}}$), and the Schmid stress on the cross-slip plane ($\sigma_{\mathrm{s}}^{\mathrm{c}}$). However, for every case studied at most one of the three stress components is non-zero. In this paper, we extend the work of Kang et al. [22] and consider the general case in which all three stress components can be non-zero. The large number of possible stress combinations is the main challenge that we face in this work. We also extend the range of stress to higher magnitudes, which are found to be necessary to realize the Fleischer mechanism.

The rest of this paper is organized as follows. Section 2 discusses the simulation setup and the range of stress configurations considered in the study. Section 3 gives the results of the energy barrier predictions for both the FE and Fleischer mechanisms. Section 4 discusses the results and extracts an analytic expression suitable for mesoscale (DD) simulations. The expression for the energy barrier as a function of the stress tensor naturally leads to an activation volume tensor, whose mathematical properties are discussed. A mechanism map is constructed to delineate the regions in the stress space in which the FE mechanism and the Fleischer mechanism operate, respectively. A brief summary is given in Section 5.

2. Methods

Much of the simulation setup is the same as in the previous work [22]. An embedded-atom method (EAM) potential for Ni, named "vnih", is adopted, which was developed using the Voter and Chen format and used by Rao et al. [7, 8, 9, 10, 11, 12, 13]. This potential is chosen because its stacking fault energy prediction is close to the experimental value. The simulation cell starts as a perfect FCC crystal with 345,600 Ni atoms with a lattice constant of $a_0 = 3.52\,\text{Å}$. The cell dimensions are $30[1\bar{1}0] \times 30[111] \times 20[\bar{1}\bar{1}2]$ along the x-, y-, and z-axes, respectively. Periodic boundary conditions are applied in the x and z directions, while the y direction has (initially) traction free boundaries (until external stresses are applied at a later stage). A left-handed screw (LHS) dislocation with Burgers vector $\mathbf{b} = \frac{a_0}{2}[\bar{1}10]$ and line direction along the positive x-axis is then introduced into the crystal.

In preparation for the MEP search, we create three atomistic configurations, namely States A, $\mathrm{B}'_{\mathrm{FE}}$, and B'_{F}, in which the screw dislocation assumes various core structures. In State A, the screw dislocation is entirely dissociated on the glide plane, i.e. the (111) plane. In State $\mathrm{B}'_{\mathrm{FE}}$ a section of the dislocation is dissociated on the cross-slip plane, i.e. the $(11\bar{1})$ plane, while the rest remain dissociated on the glide plane. This is an intermediate

configuration if the dislocation cross-slips by the FE mechanism, as shown in Figure 1(a). In State B'_F a section of the leading partial on the glide plane dissociates into a Shockley partial on the cross-slip plane and a stair-rod dislocation. This is an intermediate configuration if the dislocation cross-slips by the Fleischer mechanism, as shown in Figure 1(b). More details of how to create the atomistic configurations for States A, B'_{FE}, and B'_F can be found in Appendix A. The cross-slipped section in States B'_{FE} and B'_F are sufficiently long that if they were allowed to relax (by energy minimization) the entire dislocation would spread on the cross-slip plane and eventually escape the crystal from the surface. Therefore, the States B'_{FE} and B'_F are relaxed using the conjugate gradient algorithm only for 5 to 40 steps. State A, on the other hand, is relaxed to the local energy minimum.

A screw dislocation undergoing cross-slip is coupled with four shear stress components. They are the Schmid (s) and Escaig (e) stresses on both the glide plane (g) and cross-slip plane (c), as shown in Figure 1(a). On the given plane (g or c), the Schmid stress moves both partials in the same direction and the Escaig stress moves the two partials in opposite directions. We choose the sign convention that the Escaig stress is positive if it pulls the two partials away from each other, i.e. increases the stacking fault width on the given plane. Within the chosen coordinate system, these stresses can be expressed in terms of Cartesian stress components as follows.

$$\sigma_s^g = \sigma_{xy} \tag{1}$$

$$\sigma_e^g = \sigma_{yz} \tag{2}$$

$$\sigma_s^c = \frac{2\sqrt{2}\sigma_{xz} - \sigma_{xy}}{3} \tag{3}$$

$$\sigma_e^c = \frac{7\sigma_{yz} + 2\sqrt{2}\,(\sigma_{zz} - \sigma_{yy})}{9}. \tag{4}$$

In the coupled set of equations, there are five Cartesian stress components on the right-hand side, but only four stress components on the left-hand side. We enforce a supplementary condition of $\sigma_{zz} = -\sigma_{yy}$ to enable a one-to-one mapping between Cartesian stress components and the Escaig/Schmid stress components on the two planes. Due to the boundary conditions (periodic in x and z, free surface in y), the stress components σ_{xz} and σ_{zz} are imposed by adjusting the shape of the simulation cell (i.e. applying strain), while the stress components σ_{xy}, σ_{yy}, and σ_{yz} are imposed by applying external forces on surface atoms. To avoid surface effects on the evaluation of stress, the stress is calculated as the sum of the Virial stress contributions over an interior region away from the two surfaces; this region is defined as the group of atoms whose y-coordinate is within (-36 Å, 36 Å) in the perfect crystal structure before the dislocation is introduced.

With the external forces are applied to the surface atoms, we iteratively adjust the simulation cell shape containing the dislocation in State A and perform energy minimization, until the simulation cell reaches both the desired stress condition and energy minimum (stress error below ± 0.05 MPa, energy difference below 10^{-9} eV). State B′ (B'_F or B'_{FE}) is then further relaxed for 5 to 10 steps under the same external forces and cell shape as State A under the

same stress condition.

3. Results

Using a modified version of the string method [22, 23, 24, 25], we obtain the MEP of cross-slip under a large number of stress combinations using the MD++ simulation program [26] developed by the authors. The workflow for creating the dislocation configurations and managing the MEP relaxations under all stress conditions is available in the form of a Python notebook as part of the MD++ installation. Because the dislocation in State A would not be stationary unless the Schmid stress on the glide plane is zero, we require $\sigma_{\mathrm{s}}^{\mathrm{g}} = 0$ in all the calculations. (See Section 4.4 for a discussion of the effect of $\sigma_{\mathrm{s}}^{\mathrm{g}}$ within the context of the "invisible obstacles" hypothesis.) To investigate the FE mechanism, we obtain the MEP for cross-slip when the initial path is constructed from a linear interpolation between State A and State $\mathrm{B}'_{\mathrm{FE}}$. This calculation is performed for $6 \times 6 \times 5 = 180$ stress combinations in which each of the magnitudes of $\sigma_{\mathrm{e}}^{\mathrm{g}}$ and $\sigma_{\mathrm{e}}^{\mathrm{c}}$ varies among 0, 0.2, 0.4, 0.6, 0.8 and 1 GPa, and the magnitude of $\sigma_{\mathrm{s}}^{\mathrm{c}}$ varies among 0, 0.2, 0.4, 0.6 and 0.8 GPa. In these simulations, $\sigma_{\mathrm{e}}^{\mathrm{g}}$ is negative (when it is non-zero), to promote constriction of the stacking fault while $\sigma_{\mathrm{e}}^{\mathrm{c}}$ is positive (when it is non-zero) to promote expansion of the stacking fault on the cross-slip plane. In our simulations, $\sigma_{\mathrm{s}}^{\mathrm{c}}$ is negative (when it is non-zero), though both positive and negative Schmid stresses on the cross-slip plane are expected to promote cross-slip. Each MEP relaxation is performed for 800 steps (which takes 8 hours on 24 cores) and is considered converged if (1) the slope of the linear fit of energy barrier over the last 400 steps is less than 10^{-5} eV/step; and (2) the mean squared error of the linear fit is less than 10^{-3} $(\mathrm{eV})^2$. If convergence is not reached, the MEP relaxation is restarted for another 400 steps. If the energy barrier during relaxation becomes negative, we consider the calculation has failed to converge. All these 180 simulations (whose initial paths are constructed based on the FE mechanism) converge to MEPs that are consistent with the FE mechanism.

To investigate the Fleischer mechanism, we obtain the MEP with initial path constructed based on the Fleischer mechanism, for 72 stress combinations with $-\sigma_{\mathrm{e}}^{\mathrm{g}} = 0$, 0.4, 0.8, and 1.2 GPa, $\sigma_{\mathrm{e}}^{\mathrm{c}} = 0$, 0.4, 0.8, 1.2, 1.6, and 2 GPa, and $-\sigma_{\mathrm{s}}^{\mathrm{c}} = 1.6$, 1.8, and 2 GPa. However, converged energy barrier data was obtained for only 44 of these stress conditions. For the other 28 stress conditions, State A is not stable and spontaneously cross-slips and escapes to the surface. These cases are considered to have zero energy barrier for cross slip, and thus not included in the results. All the 44 simulations converge to MEPs that are consistent with the Fleischer mechanism.

To study the competition between the Fleischer and FE mechanisms, the 224 stress conditions (180 for FE and 44 for Fleischer) for which converged energy barriers were obtained were simulated again with the initial path corresponding to both FE and Fleischer mechanisms. The initial path for the FE(Fleischer) mechanism was constructed from a linear interpolation between State A and State $\mathrm{B}'_{\mathrm{FE}}(\mathrm{B}'_{\mathrm{F}})$. In the string method employed here, the State (B') at the right end of the string is allowed to change during the relaxation.

As a result, even if the initial path is set up according to one (e.g. FE) mechanism, it is possible for the relaxed MEP to converge to a different (e.g. Fleischer) mechanism. Among the 224 stress conditions considered here, 177 FE cases and 44 Fleischer cases converged to their corresponding mechanism no matter which mechanism was selected when the initial path was constructed. The other 3 FE cases, where $(-\sigma_e^g, \sigma_e^c, -\sigma_s^c) = (0.8, 1.0, 0.8), (1.0, 1.0, 0.8), (1.0, 0.8, 0.8)$ GPa, converged to different mechanisms depending on which initial path was selected, and the converged energy barrier values are very close between the two mechanisms. Therefore, we consider these three stress conditions to be at the boundary between the two stress domains in which the FE and Flesicher mechanisms dominate, respectively.

To determine the boundary between the FE and Fleischer mechanisms more accurately, two additional sets of simulations were performed under the stress condition of: (1) $-\sigma_e^g = 0.4$ GPa, $\sigma_e^c = 0$, 0.2, 0.4, 0.6, 0.8, 1.0 GPa, and $-\sigma_s^c = 1.1$, 1.2, 1.3, 1.4, 1.5 GPa; (2) $-\sigma_s^c = 1.0$ GPa, σ_e^c and $-\sigma_e^g$ varies in 0, 0.2, 0.4, 0.6, 0.8, 1.0 GPa; using initial paths constructed from both mechanisms.

3.1. Energy profile and saddle configurations

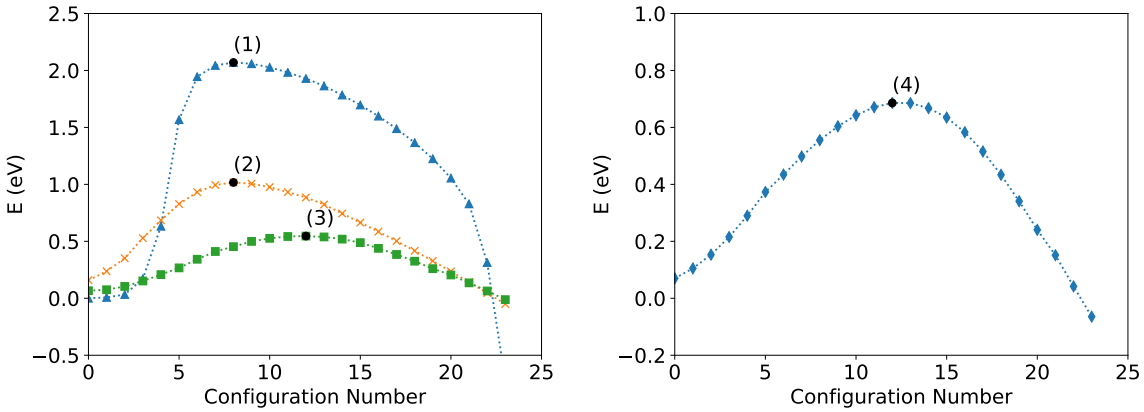

Figure 2. Energy profile along relaxed MEPs for cross-slip under several stress conditions. The circles mark the saddle configuration with the maximum energy along the MEP and hence the energy barrier. (a) Examples where the final MEPs are consistent with the FE mechanism. Triangles (1): $\sigma_e^g = 0$, $\sigma_s^c = -0.2$ GPa, $\sigma_e^c = 0$. Crosses (2): $\sigma_e^g = -0.4$ GPa, $\sigma_s^c = -0.4$ GPa, $\sigma_e^c = 0.6$ GPa. Squares (3): $\sigma_e^g = -1$ GPa, $\sigma_s^c = -0.8$ GPa, $\sigma_e^c = 0.4$ GPa. (b) An example where the final MEP is consistent with the Fleischer mechanism. Diamonds (4): $\sigma_e^g = 0$, $\sigma_s^c = -2$ GPa, $\sigma_e^c = 0.4$ GPa.

Figure 2(a) plots the energy profile along relaxed MEPs under several stress conditions in which the FE mechanism operates. Figure 2(b) plots the energy profile under a stress condition in which the Fleischer mechanism operates. The maximum energy points along

these MEPs are marked by a circle; they correspond to energy barriers for cross-slip and the corresponding atomistic configurations are shown in Figure 3.

Figure 3(a) shows the saddle configuration for cross-slip under stress condition (1): $\sigma_{\mathrm{e}}^{\mathrm{g}} = 0$, $\sigma_{\mathrm{s}}^{\mathrm{c}} = -0.2$ GPa, $\sigma_{\mathrm{e}}^{\mathrm{c}} = 0$. Even though Schmid stress on the cross slip plane is the only non-zero stress component, the saddle configuration clearly shows the FE mechanism, in which two constriction points are formed on the glide plane with a cross-slipped segment in between. This behavior is observed typically under low stress conditions.

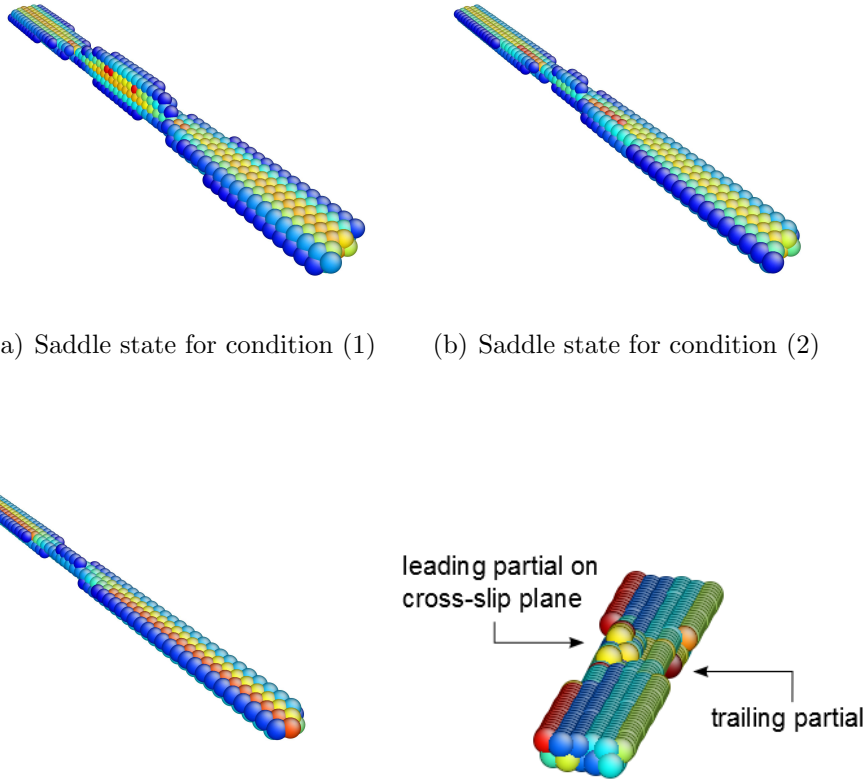

(a) Saddle state for condition (1) (b) Saddle state for condition (2)

(c) Saddle state for condition (3) (d) Saddle state for condition (4)

Figure 3. Atomistic structures of the dislocation core during cross-slip under the stress conditions defined in Figure 2. Images created using AtomEye [28]. Atoms are colored according to their central symmetry deviation (CSD) [27] parameter.

Under higher stresses, the length of the cross-slipped segment becomes shorter in the saddle configuration, even when the cross-slip mechanism is still largely consistent with the FE mechanism. For example, Figure 3(b) shows the saddle configuration under stress condition (2): $\sigma_{\mathrm{e}}^{\mathrm{g}} = -0.4$ GPa, $\sigma_{\mathrm{s}}^{\mathrm{c}} = -0.6$ GPa, $\sigma_{\mathrm{e}}^{\mathrm{c}} = 0.6$ GPa. Here the re-dissociation of the screw dislocation on the cross-slip plane is not clearly visible in this saddle configuration. Figure 3(c) shows the saddle configuration under stress condition (3): $\sigma_{\mathrm{e}}^{\mathrm{g}} = -1$ GPa, $\sigma_{\mathrm{s}}^{\mathrm{c}} = -1$ GPa, $\sigma_{\mathrm{e}}^{\mathrm{c}} = 0.4$ GPa. Here the dislocation appears to be constricted along a

finite-length segment on the glide plane, similar to the mechanisms proposed by Friedel [18], Schoeck and Seeger [20], and Wolf [21]. The atomistic snapshots suggest that, under such high stress conditions, the energy barrier for cross-slip corresponds to the formation of constrictions on the glide plane, and subsequent dissociation on the cross-slip plane only causes reduction in energy. However, the atomistic snapshots need to be interpreted with care, because the image depends on the visualization algorithm that determines which atoms to plot as dislocation core atoms. Here the snapshots are created by plotting only the atoms whose central symmetry deviation (CSD) [27] parameter exceeds 1 Å^2 and excluding atoms on the top and bottom (free) surfaces.

Figure 3(d) shows the saddle configuration under stress condition (4): $\sigma_{\text{e}}^{\text{g}} = 0$, $\sigma_{\text{s}}^{\text{c}} = -2$ GPa, $\sigma_{\text{e}}^{\text{c}} = 0.4$ GPa. Here the magnitude of the Schmid stress on the cross slip plane is very large (2 GPa), to promote the Fleischer mechanism. Indeed, the saddle configurations shows that the leading partial on the cross-slip plane already forms, before the trailing partial on the glide-plane disappears, consistent with the Fleischer mechanism (see Fig. 1(b)). However, in some of the stress conditions where $-\sigma_{\text{s}}^{\text{c}}$ exceeds 1 GPa to promote the Fleischer mechanism, the saddle state seems to correspond to a FE-Fleischer hybrid mechanism [29]. Under such stress conditions it is not possible to tell, from the atomistic snapshots, whether the constriction on the glide plane occurs first or the dissociation on the cross-slip plane occurs first. We consider such stress conditions to be near the boundary between the stress domain in which the FE mechanism dominates and that in which the Fleischer mechanism dominates.

3.2. Energy barrier as a function of multiple stress components

We first examine the cross-slip energy barrier E_{b} as a function of three stress components, $\sigma_{\text{e}}^{\text{g}}$, $\sigma_{\text{s}}^{\text{c}}$, and $\sigma_{\text{e}}^{\text{c}}$, when their magnitudes vary among 6 possible values from 0 to 1 GPa. For these 216 stress conditions, the initial paths were created according to the FE mechanism, and the converged MEPs are also consistent with the FE mechanism. It is difficult to show all 216 data points on the same graph. Instead, Figure 4 plots different "slices" of the data in the stress space. In each subfigure, E_{b} is plotted as a function of one stress component (the horizontal axis), while another stress component is allowed to take 6 possible values (different symbols/curves), and the third stress component is fixed at a constant value.

Within the range of stress considered here, the energy barrier is highest when all stress components are zero, and decreases with increasing stress magnitude. Consistent with the findings in the previous work [22], the energy barrier decreases most rapidly with increasing the magnitude of the Escaig stress on the glide plane $\sigma_{\text{e}}^{\text{g}}$. The Schmid stress on the cross-slip plane $\sigma_{\text{s}}^{\text{c}}$ has the smallest (but non-negligible) effect on the energy barrier, while the Escaig stress on the cross-slip plane $\sigma_{\text{e}}^{\text{c}}$ has an effect somewhere between that of $\sigma_{\text{e}}^{\text{g}}$ and $\sigma_{\text{s}}^{\text{c}}$.

Figure 4 allows us to make a number of general observations on how the cross-slip energy barrier E_{b} depends on the three stress components: $\sigma_{\text{e}}^{\text{g}}$, $\sigma_{\text{e}}^{\text{c}}$, and $\sigma_{\text{s}}^{\text{c}}$ for the FE mechanism. We first discuss how E_{b} depends on the sign of the stress components. Recall that we have

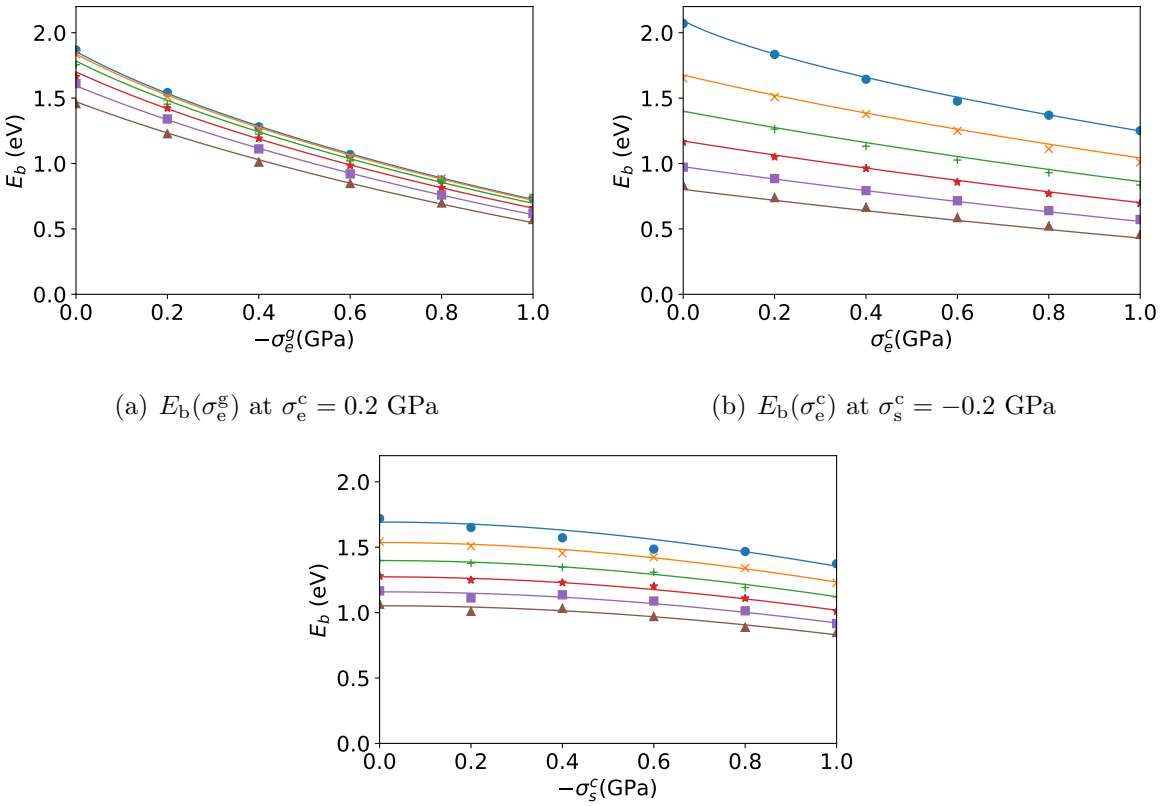

(a) $E_\mathrm{b}(\sigma_\mathrm{e}^\mathrm{g})$ at $\sigma_\mathrm{e}^\mathrm{c} = 0.2$ GPa

(b) $E_\mathrm{b}(\sigma_\mathrm{e}^\mathrm{c})$ at $\sigma_\mathrm{s}^\mathrm{c} = -0.2$ GPa

(c) $E_\mathrm{b}(\sigma_\mathrm{s}^\mathrm{c})$ at $\sigma_\mathrm{e}^\mathrm{g} = -0.2$ GPa

Figure 4. Energy barrier E_b for cross-slip plotted as a function of one of the three stress components. Symbols represent data from atomistic simulations and lines represent curve fits based on Eqs. (5) and (6). In each plot, one of the stress components is fixed, another component is along the x-axis, and the magnitude of the third component is varied according to the following convention; circles: 0, crosses: 0.2 GPa, pluses: 0.4 GPa, stars: 0.6 GPa, squares: 0.8 GPa, triangles: 1 GPa.

defined the Escaig stress to be positive if it expands the separation between the two partials. Figure 4(a) shows that E_b is reduced if $\sigma_\mathrm{e}^\mathrm{g}$ becomes more negative. This is expected because a negative $\sigma_\mathrm{e}^\mathrm{g}$ compresses the two partials toward each other on the glide plane, making it easier to form a constriction. Figure 4(b) shows that E_b is reduced if $\sigma_\mathrm{e}^\mathrm{c}$ becomes more positive. This is expected because a positive $\sigma_\mathrm{e}^\mathrm{c}$ expands the stacking fault on the cross-slip plane, thus lowering the dislocation core energy on the cross-slip plane. Because E_b depends on the sign of $\sigma_\mathrm{e}^\mathrm{g}$ and $\sigma_\mathrm{e}^\mathrm{c}$, the derivatives of E_b with respect to these two stress components are non-zero at the zero-stress condition. The data shown in Figure 4(a) and Figure 4(b) also appear to be a convex function, i.e. the second derivatives of E_b with respect to $\sigma_\mathrm{e}^\mathrm{g}$ and $\sigma_\mathrm{e}^\mathrm{c}$ seems to be positive in the range of stress considered.

On the other hand, from Figure 4(c) E_b appears to be a concave function of $\sigma_\mathrm{s}^\mathrm{c}$ and has a zero-slope when $\sigma_\mathrm{s}^\mathrm{c} = 0$. This is consistent with the behavior expected from the line-tension model, in which E_b is independent of the sign of $\sigma_\mathrm{s}^\mathrm{c}$. Because a large Schmid stress

magnitude on the cross-slip plane, regardless of sign, would induce the dislocation to bow out on the cross-slip plane, it is reasonable to assume that E_b is an even function of $\sigma_\mathrm{s}^\mathrm{c}$.

4. Discussion

4.1. Analytic approximation of $E_\mathrm{b}(\sigma_\mathrm{e}^\mathrm{g}, \sigma_\mathrm{e}^\mathrm{c}, \sigma_\mathrm{s}^\mathrm{c})$

In order to use the cross-slip energy barrier data obtained from the atomistic model as input to mesoscale DD models, it would be more convenient if the energy barrier can be expressed as an analytic function of the local stress. Ideally the chosen function would have a simple form and, at the same time, accurately represent the atomistic data. A simple functional form would not only lead to convenience in numerical implementation and higher computational efficiency, but would also make it possible to assign physical interpretations to its parameters.

We found that the following functional form results in a reasonable compromise between simplicity and accuracy. The energy barrier is written as a one-dimensional function of an effective stress, τ^*, which is a combination of the three relevant stress components, i.e.

$$E_\mathrm{b}(\tau^*) = A\left[1 - \left(\frac{\tau^*}{\tau_0}\right)^p\right]^q \tag{5}$$

$$\tau^* \quad = C_\mathrm{e}^\mathrm{g}\,\sigma_\mathrm{e}^\mathrm{g} + C_\mathrm{e}^\mathrm{c}\,\sigma_\mathrm{e}^\mathrm{c} + \left(D_\mathrm{s}^\mathrm{c}\,\sigma_\mathrm{s}^\mathrm{c}\right)^2 \tag{6}$$

where A, τ_0, p, q, C_e^g, C_e^c, and D_s^c are fitting parameters. This functional form was motivated by the observation that the isosurfaces of E_b in the three-dimensional stress space appear to be nearly planar and almost parallel to each other. Because of this, a linear combination of the stresses was initially attempted to construct τ^*. However, Figure 4(c) suggests that $E_\mathrm{b}(\tau^*)$ is an even function of $\sigma_\mathrm{s}^\mathrm{c}$. This motivates the use of a quadratic form, $\left(D_\mathrm{s}^\mathrm{c}\,\sigma_\mathrm{s}^\mathrm{c}\right)^2$, in Eq. (6). The resulting analytic expression indeed captures the behavior of the atomistic data more accurately than a linear combination of stresses for τ^*.

The fitting parameters are determined separately for the cross-slip energy barrier data corresponding to the FE and Fleischer mechanisms. Their numerical values are given in Table 1. The suitability of this functional form in describing the atomistic energy barrier data can be assessed from Figure 5, in which the atomistic data are plotted together with the fitted analytic function $E_\mathrm{b}(\tau^*)$. It is worth noting that all 177 atomistic data points discussed in Section 3 (plus 29 additional data points to be introduced in Section 4.3) corresponding to the FE mechanism collapse to a one-dimensional line (when appropriate constants C_e^g, C_e^c, and D_s^c are used), as shown in Figure 5(a). This gives strong support for the concept of the effective stress τ^* (a linear combination of the Escaig stress components and the square of the Schmid stress component) as the major controlling factor of the cross-slip energy barrier. The fitted function is also plotted on top of the atomistic data in Figure 4; good agreement is observed between the two. The small spread of the atomistic data around the fitted curve

	FE	Fleischer
A	2.1455	2.2352
τ_0	5.5949	5.5949
p	0.7288	0.7288
q	1.4428	1.4428
$C_{\mathrm{e}}^{\mathrm{g}}$	-2.1077	-2.1197
$C_{\mathrm{e}}^{\mathrm{c}}$	1.1150	1.1454
$D_{\mathrm{s}}^{\mathrm{c}}$	0.7218	0.7494

Table 1. Fitting parameters for the cross-slip energy barrier for FCC Ni corresponding to the Friedel-Escaig (FE) and Fleischer mechanisms. A is in units of eV and τ_0 is in units of GPa. The parameters $C_{\mathrm{e}}^{\mathrm{g}}$ and $C_{\mathrm{e}}^{\mathrm{c}}$ are unitless, but $D_{\mathrm{s}}^{\mathrm{c}}$ has the unit of $(\mathrm{GPa})^{-1/2}$. The parameters are p and q unitless.

in Figure 5 indicates the existence of other, less important factors influencing the cross-slip energy barrier. Given the unavoidable error in the atomistic data themselves, the quality of the fit is considered satisfactory, especially considering the simplicity of the functional form given in Eqs. (5) and (6). Generalizing the effective stress to a complete second-order polynomial of the three stress components only leads to marginal improvement in the quality of the fit at the expense of more fitting parameters and with the danger of overfitting; hence that possibility is not discussed any further.

From a practical point of view, when used as an input function to mesoscale DD models, it is often not necessary for the energy barrier function to be uniformly accurate under all stress conditions. The principle region of interest, in which the energy barrier function needs to be most accurate, is indicated by the region between the dashed lines in Figure 5, where the energy barrier lies roughly between 0.25 eV and 1 eV. When the stress is so small that the energy barrier is above this region, the cross-slip rate is so low that cross-slip is very unlikely to occur over the time-scale of interest. When the stress is so large that the energy barrier is below this region, cross-slip must have already occurred earlier when the stress was lower.

From Figure 5 it appears that the energy barrier for the homogeneous cross slip considered here can only occur at high stresses, e.g. above 2 GPa. This may give the impression that homogeneous cross slip would not occur under most deformation conditions, where the flow stress is usually lower that 1 GPa. However, the local stress experienced by the dislocations can be significantly higher than the externally applied stress. For example, the shear stress within $30\,b$ of another dislocation can exceed 2 GPa, where b is the magnitude of the Burgers vector. In addition, the entropy effects, which is not accounted for here, can increase the rate of cross slip beyond the estimates based on harmonic transition state theory, as has been demonstrated in the case of dislocation nucleation [23, 24]. Nonetheless, heterogeneous cross slip, facilitated by the pre-existing constrictions, e.g. jogs, on the screw

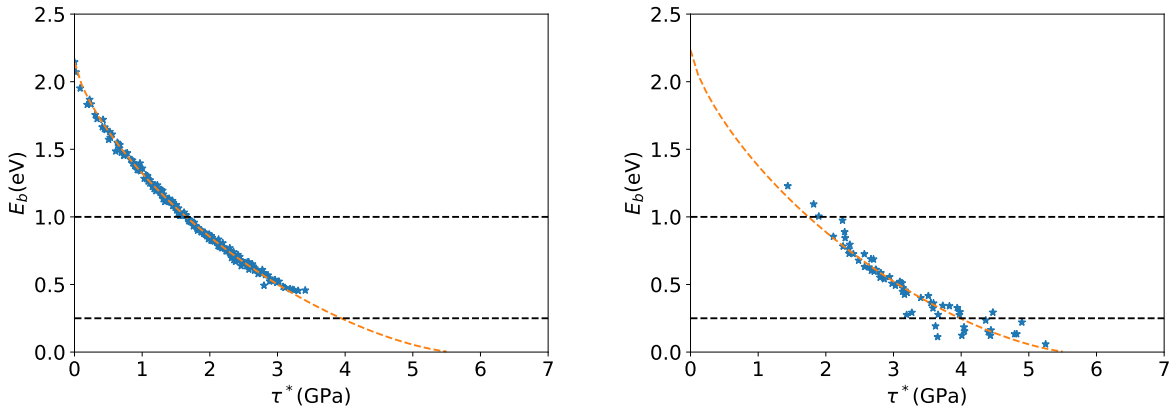

Figure 5. The fitting curves relating the effective stress τ^* to the energy barrier E_b for the (a) FE and (b) Fleischer mechanisms.

dislocation [5] and "invisible" obstacles hypothesized by Escaig [35] (see Section 4.4) can have higher rate than homogeneous cross slip.

Given that the cross slip energy barrier is a smooth function of the stress components (see Fig. 4), it seems that future work aimed at developing cross slip energy barrier functions in the form of Eqs.(5)-(6) may use a coarser grid of stress components. For example, $3 \times 3 \times 3 = 27$ atomistic calculations may be sufficient in providing data for fitting the energy barrier function, which are much fewer than the 200+ calculations performed in this work.

Based on Eqs.(6) and (2)-(4), the effective stress can be rewritten in a more compact form. Define tensorial constants C_{ij} and D_{ij} such that

$$\begin{aligned} \frac{1}{2}C_{ij}\sigma_{ij} &= C_\mathrm{e}^\mathrm{g}\sigma_\mathrm{e}^\mathrm{g} + C_\mathrm{e}^\mathrm{c}\sigma_\mathrm{e}^\mathrm{c} \\ \frac{1}{2}D_{ij}\sigma_{ij} &= D_\mathrm{s}^\mathrm{c}\sigma_\mathrm{s}^\mathrm{c} \\ \tau^* &= \frac{1}{2}C_{ij}\sigma_{ij} + \left(\frac{1}{2}D_{ij}\sigma_{ij}\right)^2 \end{aligned} \tag{7}$$

where the Einstein convention is assumed where the repeated indices (i and j) are summed over from 1 to 3. In our atomistic model, we have considered a left-handed screw dislocation with $\frac{a_0}{2}[\bar{1}10]$ Burgers vector cross-slipping from the (111) plane to the $(11\bar{1})$ plane. Using the crystal coordinate system, in which the x-, y-, z-axes correspond to the $[1\,0\,0]$, $[0\,1\,0]$, $[0\,0\,1]$ directions, respectively, the tensorial constants for the FE mechanism can be expressed as

$$\mathbf{C} = \begin{bmatrix} 0.4680 & 0.4680 & -0.7596 \\ 0.4680 & 0.4680 & -0.7596 \\ -0.7596 & -0.7596 & -0.9360 \end{bmatrix} \tag{8}$$

and

$$\mathbf{D} = \begin{bmatrix} -0.5893 & 0 & 0.2947 \\ 0 & 0.5893 & -0.2947 \\ 0.2947 & -0.2947 & 0 \end{bmatrix} \tag{9}$$

It is important at this point to note that the **C** and **D** tensors given above correspond to a left-handed screw dislocation along the $[1\bar{1}0]$ direction. Since there are 12 slip systems in an FCC crystal and we can have either left-handed screw (LHS) or right-handed screw (RHS) for each slip system, there are 24 **C** tensors and 24 **D** tensors for the FE mechanism. There are also 24 cases for the Fleischer mechanism. Using the results from this paper to calculate the appropriate energy barrier for cross-slip in a DD simulation requires identifying the correct slip system and dislocation type (LHS or RHS) and using the appropriate **C** and **D** tensors. For comparing FE and Fleischer mechanisms, one would have to calculate the energy barriers separately and choose the mechanism with the lower energy barrier.

4.2. Activation volume tensor

The negative slope of the energy barrier-stress curve, e.g. Figure 5, is usually called the activation volume. The activation volume is of significant interest because it can be measured experimentally [14, 15, 16] and thus provides a valuable benchmark for the theory of stress-driven thermally activated processes. Because the cross-slip energy barrier is influenced by multiple stress components, there is ambiguity in which stress component should be used when taking the derivative. If we write the energy barrier E_b as a function of the local stress tensor σ_{ij}, then it is natural to define a symmetric activation volume tensor,

$$\Omega_{ij} \equiv -\frac{\partial E_\mathrm{b}}{\partial \sigma_{ij}}. \tag{10}$$

When E_b can be expressed in terms of the effective stress τ^*, as in Eq.(5), we have

$$\Omega_{ij} = -\frac{\partial E_\mathrm{b}}{\partial \tau^*}\frac{\partial \tau^*}{\partial \sigma_{ij}}, \tag{11}$$

where

$$\frac{\partial E_b}{\partial \tau^*} = -\frac{A\,p\,q}{\tau_0}\left[1-\left(\frac{\tau^*}{\tau_0}\right)^p\right]^{q-1}\left(\frac{\tau^*}{\tau_0}\right)^{p-1} \quad \text{and} \tag{12}$$

$$\frac{\partial \tau^*}{\partial \sigma_{ij}} = \frac{1}{2}C_{ij} + \frac{1}{2}\left(D_{kl}\sigma_{kl}\right)D_{ij}. \tag{13}$$

It is worth pointing out some of the mathematical properties of the activation volume tensor. First, it is traceless, i.e. $\Omega_{11}+\Omega_{22}+\Omega_{33}=0$. This is because the **C** and **D** tensors are traceless, and is due to the fact that the cross-slip energy barrier only depends on the deviatoric part of the stress tensor. This is fully consistent with the fact that plasticity is

independent of the hydrostatic pressure. Another property is that $b_i\,\Omega_{ij}\,b_j = 0$, because a normal stress acting along the Burgers vector direction does not couple to any partials of the screw dislocation, so it cannot influence cross-slip. In the present case of $\mathbf{b} = \frac{a_0}{2}[1\,\bar{1}\,0]$, this leads to the condition that $\Omega_{11} + \Omega_{22} = 2\,\Omega_{12}$.

To facilitate comparison with experiments, it seems natural to define a scalar activation volume in terms of the norm of the activation volume tensor,

$$\Omega \equiv \sqrt{2\,\Omega_{ij}\Omega_{ij}} \tag{14}$$

Physically, Ω corresponds to the rate of decrease of E_b with the stress magnitude when the stress tensor σ_{ij} is parallel to Ω_{ij}. From Eqs.(11) and (14), we have

$$\Omega = -\frac{\partial E_\mathrm{b}}{\partial \tau^*}\sqrt{2\,\frac{\partial \tau^*}{\partial \sigma_{ij}}\,\frac{\partial \tau^*}{\partial \sigma_{ij}}} \tag{15}$$

which is consistent with the expectation that the activation volume is proportional to the negative slope of the energy barrier E_b with respect to the effective stress τ^*.

As an example, let us consider the special case in which $\sigma_\mathrm{s}^\mathrm{c} = 0$, so that $D_{kl}\sigma_{kl} = 0$, and $\partial\tau^*/\partial\sigma_{ij} = C_{ij}/2$. In this case,

$$\Omega = -\frac{\partial E_\mathrm{b}}{\partial \tau^*}\sqrt{\frac{1}{2}\,C_{ij}\,C_{ij}} \tag{16}$$

Given Eq.(8), we have

$$\Omega = -1.40\,\frac{\partial E_\mathrm{b}}{\partial \tau^*} \tag{17}$$

Figure 6 plots the magnitude of activation volume Ω as a function of the effective stress τ^* (for the case of $\sigma_\mathrm{s}^\mathrm{c} = 0$). The activation volume decreases with the magnitude of the effective stress. If we require the effective stress τ^* to be above 1.7 GPa, so that the energy barrier is below 1 eV (see Figure 5), then Ω is below $7\,b^3$. This is much lower than previous estimates from experimental results, and somewhat lower compared with previous simulation results, as shown in Table 2. If we ignore the constraint on the effective stress, then the activation volume in the low stress limit exceeds $30\,b^3$, and falls within the range of previously reported values of Ω from simulations. The discrepancy between experimental and computational estimates of the activation volume suggests that processes other than homogeneous cross-slip are controlling the experiments which are designed to probe cross-slip behaviors.

4.3. Competition between Friedel-Escaig and Fleischer mechanisms

In order to delineate the stress domains in which the FE and Fleischer mechanisms operate, respectively, we performed additional MEP calculations under stress conditions expected to be near the boundary between the two domains. Because we have found that the Fleischer

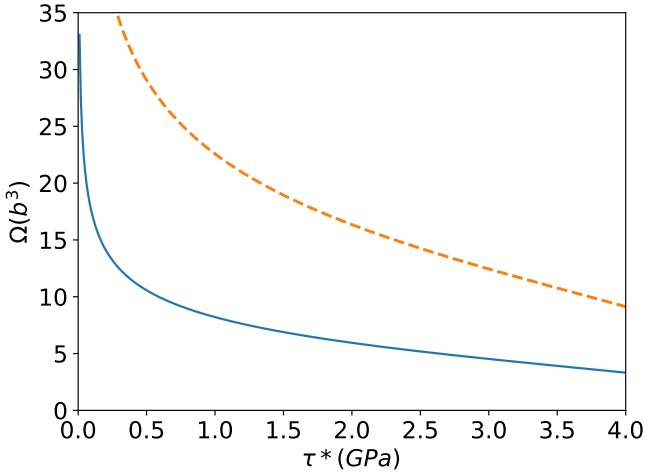

Figure 6. Activation volume for cross-slip by the FE mechanism in nickel as a function of the "effective stress" τ^* in the case of $\sigma_s^c = 0$ (solid line), based on the energy barrier expression in Eqs.(5) and (6). Dashed line corresponds to the case where the effect of Schmid stress on the glide plane is accounted for with the introduction of "invisible" obstacles (see Section 4.4).

Table 2. Activation volume estimates for cross slip in copper, all in units of b^3.

	Experiments		Simulations			
	Bonneville [16]	Duesberry [30]	Saada [31]	Rao [7]	Rao [32]	Rasmussen [33]
Ω	280	300	42	10-20	60	15

mechanism does not operate unless $|\sigma_s^c|$ exceeds 0.8 GPa, we performed two sets of simulations under the following conditions: (1) $-\sigma_s^c = 1.1$, 1.2, 1.3, 1.4, 1.5 GPa; $\sigma_e^c = 0$, 0.2, 0.4, 0.6, 0.8, 1.0 GPa; and $-\sigma_e^g = 0.4$ GPa; (2) let both $-\sigma_e^g$ and σ_e^c span the range of 0, 0.2, 0.4, 0.6, 0.8, 1.0 GPa; and $-\sigma_e^g = 1.0$ GPa. Figure 7(a) displays the outcomes from these simulations. Stars indicate the stress conditions where the FE mechanism operate, and squares indicate the stress conditions where the Fleischer mechanism operate, regardless of whether the initial path is constructed based on the FE or the Fleischer mechanism. The symbols (stars or squares) are not shown for conditions in which the mechanism of the converged MEP depends on the mechanism of the initial path, i.e. initial path of FE converges to FE mechanism, and initial path of Fleischer converges to Fleischer mechanism.

The hatched region in Figure 7(a) shows the stress region in which the fitted energy barrier function for the Fleischer mechanism is lower than that for the FE mechanism. Recall that the coefficients for the energy barrier function for the FE mechanism were fitted to the 177 data points for which all stress components are no larger than 1 GPa. The coefficients for the energy barrier function for the Fleischer mechanism are fitted to the (much fewer) atomistic data that show the Fleischer mechanism, as well as to satisfy the constraint that

the resulting domain boundary with the FE mechanism is consistent with the atomistic data. The latter constraint includes the 2D domain map shown in Figure 7(a), as well as the 177 cases that are converged to FE mechanism.

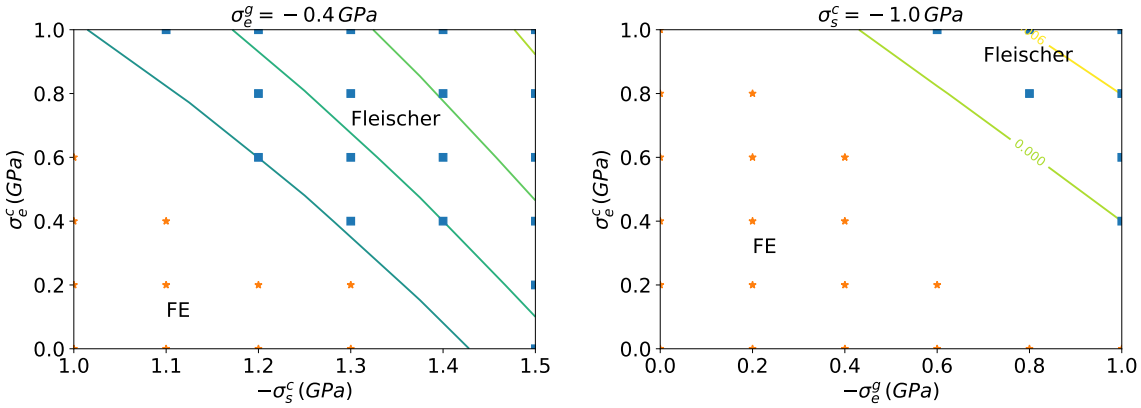

(a) 2D map

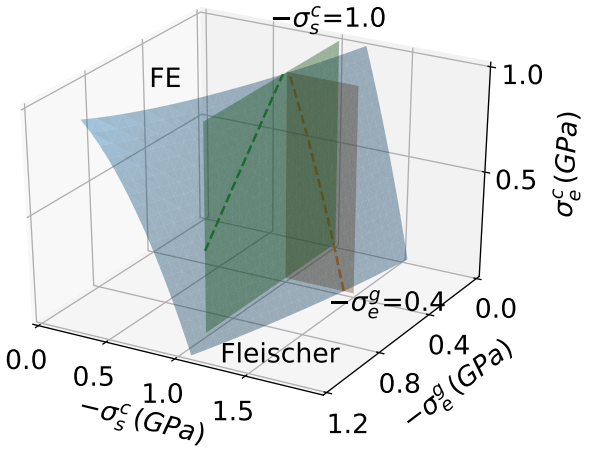

(b) 3D map

Figure 7. Maps in stress domain delineating regions in which the FE mechanism and the Fleischer mechanism operate, respectively. (a) Two-dimensional map in the space of σ_e^c and σ_s^c, with $-\sigma_e^g = 0.4$ GPa, and the map in the space of σ_e^c and σ_e^g, with $-\sigma_s^c = 1.0$ GPa. The hashed region is where the Fleischer mechanism operate, and the empty region is where the FE mechanism operate. Squares indicate stress conditions in which the Fleischer mechanism is observed in atomistic simulations; crosses indicate conditions in which the FE mechanism is observed. (b) Three-dimensional map based on the energy barrier functions given in Eqs.(5) and (6), and coefficients given in Table 1. The curved boundary is the isosurface on which the two energy barriers are equal. The lines on the isosurface are intersections with planes corresponding to the two-dimensional maps shown in (a).

Figure 7(b) shows the stress domain boundary between the FE and the Fleischer

mechanisms in 3D. The slighted curved surface is the isosurface on which the magnitude of the fitted energy function for the FE mechanism equals to that for the Fleischer mechanism. It can be seen that the FE mechanism dominates if the Escaig stress on the glide plane, $\sigma_{\mathrm{e}}^{\mathrm{g}}$, is the dominant stress component. In fact, the Fleischer mechanism operates only if the magnitude of the Schmid stress on the cross slip plane, $\sigma_{\mathrm{s}}^{\mathrm{c}}$, exceeds 1 GPa. Given a sufficiently large $|\sigma_{\mathrm{s}}^{\mathrm{c}}|$, the competition between the two mechanisms can be influenced (to a smaller extent) by the other two stress components. Increasing $-\sigma_{\mathrm{e}}^{\mathrm{c}}$ can help induce the transition to the Fleischer mechanism at a smaller $|\sigma_{\mathrm{s}}^{\mathrm{c}}|$.

4.4. Effect of Schmid stress on original glide plane

We have omitted the effect of the Schmid stress on the glide plane, $\sigma_{\mathrm{g}}^{\mathrm{s}}$ in our calculations and analyses so far. Given that Kubin, et al. [34] have proposed that $\sigma_{\mathrm{g}}^{\mathrm{s}}$ is actually the most important stress component for cross slip, a discussion of the effect of this stress component is warranted here. Intuitively, if $\sigma_{\mathrm{g}}^{\mathrm{s}}$ is non-zero, the screw dislocation would simply move on the original glide plane without the need to cross slip. However, Escaig [35] proposed that there may be obstacles that may prevent the motion of the screw dislocation on the glide plane. These obstacles are "invisible" in the sense that their stress fields are not accounted for in the calculation of $\sigma_{\mathrm{g}}^{\mathrm{s}}$. Nonetheless, the application of $\sigma_{\mathrm{g}}^{\mathrm{s}}$, in the presence of an obstacle to block glide, would result in a shrinking of the stacking fault region. The effect is the same as when a negative $\sigma_{\mathrm{g}}^{\mathrm{e}}$ is applied. Therefore, we propose that, if one adopts the line of reasoning of Escaig and Kubin, the effect of Schmid stress on the glide plane can be accounted for modifying the effective stress expression, Eq. (6), to

$$\tau^* = C_{\mathrm{e}}^{\mathrm{g}}\,\sigma_{\mathrm{e}}^{\mathrm{g}} + |C_{\mathrm{s}}^{\mathrm{g}}\,\sigma_{\mathrm{s}}^{\mathrm{g}}| + C_{\mathrm{e}}^{\mathrm{c}}\,\sigma_{\mathrm{e}}^{\mathrm{c}} + (D_{\mathrm{s}}^{\mathrm{c}}\,\sigma_{\mathrm{s}}^{\mathrm{c}})^2 \tag{18}$$

where

$$C_{\mathrm{s}}^{\mathrm{g}} = \sqrt{3}\,C_{\mathrm{e}}^{\mathrm{g}}. \tag{19}$$

because the magnitude of the screw component of the partial Burgers vector is a factor of $\sqrt{3}$ of that of the edge component. The absolute value is used for the $\sigma_{\mathrm{s}}^{\mathrm{g}}$ term because in the presence of the obstacle the stacking fault will be compressed regardless of the sign of the Schmid stress on the glide plane. With this modification of the effective stress τ^*, the $\mathbf{C}$ tensor defined in Eq. (7) will be modified, while the $\mathbf{D}$ tensor remain unchanged. This will lead to an increase of the activation volume, as shown in Figure 6 (dashed line).

5. Conclusion

We have calculated the energy barrier for cross-slip in FCC nickel by searching for minimum energy paths in an atomistic model under a large number of $\sigma_{\mathrm{e}}^{\mathrm{g}}$, $\sigma_{\mathrm{s}}^{\mathrm{c}}$, and $\sigma_{\mathrm{e}}^{\mathrm{c}}$ stress conditions. We considered two cross-slip mechanisms: the Friedel-Escaig mechanism and the Fleischer mechanism. For both mechanisms, the Escaig stress on the glide plane, $\sigma_{\mathrm{e}}^{\mathrm{g}}$, has the dominant

effect on the energy barrier, while the Schmid stress on the cross slip plane, σ_s^c, has the smallest effect. This finding is consistent with the previous report on the FE mechanism [22]. For each mechanism, the energy barrier as a function of the three stress components can be well described by a one-dimensional function of an effective stress, τ^*. The domain boundary in the stress space separating the FE-dominated regime and the Fleischer-dominated regime is determined from atomistic data. Increasing the magnitude of the Schmid stress on the cross slip plane, σ_s^c, has the dominant effect in inducing the transition from the FE mechanism to the Fleischer mechanism.

Acknowledgment

This work was supported by the U.S. Department of Energy, Office of Basic Energy Sciences, Division of Materials Science and Engineering under Award No. DE-SC0010412.

References

[1] Püschl, W. Models for dislocation cross-slip in close-packed crystal structures: a critical review. Prog. Mater. Sci. **47**, 415 (2002).
[2] Jackson, PJ. Dislocation modelling of shear in F.C.C crystals. Prog. Mater. Sci. **29**, 139 (1985).
[3] Suresh, S. Fatigue of Materials, second ed., Cambridge University Press (2004).
[4] Arsenlis, A; Cai, W; Tang, M; Rhee, M; Oppelstrup, T; Hommes, G; Pierce, TG and Bulatov, VV. Enabling strain hardening simulations with dislocation dynamics, Model. Simul. Mater. Sci. Eng. **15** 553 (2007).
[5] Vegge, T; Rasmussen, T; Leffers, T; Pedersen, OB; and Jacobsen, KW. Atomistic simulations of cross-slip of jogged screw dislocations in copper. Philos. Mag. Lett. **81**, 137 (2001).
[6] Washburn, J. Intersection cross slip. Appl. Phys. Lett. **7**, 183 (1965).
[7] Rao, S; Parthasarathy, TA; and Woodward, C. Atomistic simulation of cross-slip processes in model fcc structures. Philos. Mag. A **79**, 1167 (1999).
[8] Rao, SI; Dimiduk, DM; El-Awady, JA; Parthasarathy, TA; Uchic, MD; and Woodward, C. Atomistic simulations of cross-slip nucleation at screw dislocation intersections in face-centered cubic nickel. Philos. Mag. **89**, 3351 (2009).
[9] Rao, SI; Dimiduk, DM; El-Awady, JA; Parthasarathy, TA; Uchic, MD; and Woodward, C. Activated states for cross-slip at screw dislocation intersection in face-centered cubic nickel and copper via atomistic simulation. Acta Mater. **58**, 5547 (2010).
[10] Rao, SI; Dimiduk, DM; Parthasarathy, TA; El-Awady, JA; Woodward, C; and Uchic, MD. Calculations of intersection cross-slip activation energies in fcc metals using nudged elastic band method. Acta Mater. **59**, 7135 (2011).
[11] Rao, SI; Dimiduk, DM; Parthasarathy, TA; Uchic, MD; and Woodward, C. Atomistic simulations of intersection cross-slip nucleation in $L1_2$ Ni_3Al. Scripta Mater. **66**, 410 (2012).
[12] Rao, SI; Dimiduk, DM; El-Awady, JA; Parthasarathy, TA; Uchic, MD; and Woodward, C. Spontaneous athermal cross-slip nucleation at screw dislocation intersections in FCC metals and $L1_2$ intermetallics investigated via atomistic simulations. Philos. Mag. **93**, 3012 (2013).

[13] Rao, SI; Dimiduk, DM; Parthasarathy, TA; Uchic, MD; and Woodward, C. Atomistic simulations of surface cross-slip nucleation in face-centered cubic nickel and copper. Acta Mater. **61**, 2500 (2013).
[14] Bonneville, J. Etude de paramètres d'activation du glissement dévié dans le cuivre (Ph.D. thesis). École Polytechnique Fédérale de Lausanne (1985).
[15] Bonneville, J. and Escaig, B. Cross-slipping process and the stress-orientation dependence in pure copper. Acta Metall. **27**, 1477 (1979).
[16] Bonneville, J; Escaig, B; and Martin, JL. A study of cross-slip activation parameters in pure copper. Acta Metall. **36**, 1989 (1988).
[17] Fleischer, RL. Cross slip of extended dislocations. Acta Metall. **7**, 134 (1959).
[18] Friedel, J. Internal stresses and fatigue in metals. Editors: Rassweiler, GM and Grube, WL. Amsterdam: Elsevier, p. 220 (1959).
[19] Yoshinaga, H, and Horiuchi, R. Trans. Jpn. Inst. Met. **5**, 14 (1963).
[20] Schoeck, G, and Seeger, A. Conference "Defects in Crystalline Solids," p. 340, Bristol (1954). London: The Physical Society (1955).
[21] Wolf, HZ. Naturforsch **15a**, 180 (1960).
[22] Kang, K; Yin, J; and Cai, W. Stress dependence of cross slip energy barrier for face-centered cubic nickel. J. Mech. Phys. Solids **62**, 181 (2014).
[23] Ryu, S; Kang, K; and Cai, W. Entropic effect on the rate of dislocation nucleation. Proc. Natl. Acad. Sci. **108**, 5174 (2011).
[24] Ryu, S; Kang K; and Cai, W. Predicting the Dislocation Nucleation Rate as a Function of Temperature and Stress, J. Mater. Res. **26**, 2335 (2011).
[25] Kuykendall, WP. Investigating Strain Hardening by Simulations of Dislocation Dynamics, PhD Thesis, Stanford University (2015).
[26] The MD++ simulation program. `http://micro.stanford.edu/MDpp/`
[27] Kelchner, CL; Plimpton, SJ; and Hamilton, JC. Dislocation nucleation and defect structure during surface indentation. Phys. Rev. B **58**, 17, 11085 (1998).
[28] Li, J. AtomEye: an efficient atomistic configuration viewer. Model. Simul. Mater. Sci. Eng. **11**, 173 (2003).
[29] Pendurti, S; Juna S; Lee IH. Cooperative atomic motions and core arrangement in dislocation cross slip. Appl. Phys. Lett. **88**, 201908 (2006).
[30] Duesberry, MS; Louat, NP; Sadananda, K. The mechanics and energetics of cross-slip. Acta Metall. Mater. **40**, 149 (1992).
[31] Saada, G. Cross-slip and work hardening of f.c.c. crystals. Mater. Sci. and Eng.: A **137**, 177 (1991).
[32] Rao, SI; Dimiduk, DM; Woodward, C; and Parthasarathy, TA. On the Escaig obstacle hypothesis for cross-slip in face-centered-cubic materials. Phil. Mag. Lett. **91**, 452 (2011).
[33] Rasmussen, T; Vegge, T; Leffers, T; Pedersen, OB; and Jacobsen, KW. Simulation of structure and annihilation of screw dislocation dipoles. Phil. Mag. A, **80**, 1273 (2000).
[34] Kubin, LP; Canova, G; Condat, M; Devincre, B; Pontikis, V; and Bréchet, Y. Solid State Phenom. **23-24**, 455-472 (1992).
[35] Escaig, B. Sur le glissement dévié des dislocations dans la structure cubique à faces centrées. J. Phys. **29**, 255 (1968).
[36] Cai, W; Bulatov, VV; Chang, J; Li, J; Yip, S. Periodic Image Effects in Dislocation Modeling, Philos. Mag. A, **83**, 539 (2003).
[37] Barnett, DM. The displacement field of a triangular dislocation loop, Philos. Mag. A, **51** 383 (1985).
[38] Barnett, DM; Balluffi, RW. The displacement field of a triangular dislocation loop – a correction with commentary, Philos. Mag. Lett. **87**, 943 (2007).
[39] Van Oosterom, A; Strackee, J. The solid angle of a plane trangle, IEEE Trans. Biomedical Engr. BME-**30**, 125 (1983).

Appendix A. Procedures for Creating Atomistic Configurations

In this appendix, we describe the procedure to create the atomistic configurations containing the screw dislocation in different states needed to perform the energy barrier calculations. The script files for creating the dislocation configurations in this paper are available in MD++. [26] We first create a configuration containing a non-dissociated left-handed screw (LHS) dislocation, called State 0, using the following procedure. Starting from a perfect crystal, a dislocation dipole is inserted where the LHS dislocation is located at the center of the simulation cell (along the x-axis), and the opposite dislocation, i.e. a right-handed screw (RHS), is offset by $-L_y/2$ relative to the LHS along the y-axis, where L_y is the simulation cell size in the y direction. Note that the RHS dislocation is outside the free surface of the crystal, so that it will vanish after the atomistic configuration is relaxed (but the atomic positions are unrelaxed in State 0). To create State 0, the atoms are displaced from the perfect lattice position according to the displacement field of a Volterra dislocation dipole subjected to periodic boundary conditions in y and z directions (with cut plane being the x-y plane connecting the two dislocations). Care must be taken to avoid the conditional convergence problem in summing the displacement field from the image dislocation dipoles [36].

To create State A, in which the LHS dislocation is dissociated on the (111), i.e. x-z, plane, we further displace the atoms in State 0 according to the displacement of a Shockley partial dislocation dipole on the (111) plane. The positive partial dislocation in this dipole will become the leading partial of the dissociated dislocation, and the negative partial dislocation will react with the perfect LHS dislocation to become the trailing partial of the dissociated dislocation. Note that the perfect lattice positions $\mathbf{X}$ are always used as the input argument to evaluate the displacement field $\mathbf{u}(\mathbf{X})$ of the dislocations.

To create State $\mathrm{B}'_{\mathrm{FE}}$, in which the middle section of the LHS dislocation dissociates onto the $(11\bar{1})$, i.e. cross-slip plane, while the remaining part of the dislocation dissociates onto the (111) plane, we further displace the atoms in State 0 according to the displacement field of three partial dislocation loops. The dislocation loop near the center of the LHS dislocation is on the $(11\bar{1})$ plane. The superposition of this partial dislocation loop with the original LHS dislocation causes the middle section of the LHS dislocation to dissociate on the $(11\bar{1})$ plane. The two remaining dislocation loops on the two sides of the first loop is on the (111) plane. The superposition of these two partial dislocation loops with the original LHS dislocation causes the remaining sections of the LHS dislocation to dissociate on the (111) plane. The displacement field of an arbitrary dislocation loop can be constructed from superpositions of the displacement fields of triangular loops [37, 38, 39]. After relaxing the atomistic configuration for a given number of steps, the result is a dislocation structure shown in Figure 1(a).

To create State B'_{F}, in which the middle section of the LHS dislocation dissociates onto both the (111) and the $(11\bar{1})$ planes, forming a 3-dimensional structure, we further displace the atoms in State A according to the displacement field of a partial dislocation loop. This dislocation loop is located near the center of the LHS dislocation and is on the $(11\bar{1})$ plane.

The superposition of this partial dislocation loop with the dissociated LHS dislocation causes the middle section of the LHS dislocation to dissociate on both planes. After relaxing the atomistic configuration for a given number of steps, the result is a dislocation structure shown in Figure 1(b).

The configuration shown in Figure 1(b) corresponds to the "acute" variant of the Fleischer mechanism, meaning that the two stacking fault areas in the saddle configuration form an acute angle with each other. We also investigated the "obtuse" variant of the Fleischer mechanism, in which the two stacking fault areas form an obtuse angle with each other (e.g. when cross slip is initiated from the trailing partial on the original glide plane). We found that the "obtuse" variant always has either the same or higher energy barrier than the "acute" variant under the same stress. Therefore, here we only focus on the "acute" variant of the Fleischer mechanism, assuming that the dislocation prefers the mechanism with lower energy barrier during cross slip.